Tensile ductility of extruded aluminium alloy AA6063 in different tempers

M. Khadyko[a], D. Morin[a,b], T. Børvik[a,b] and O.S. Hopperstad[a,b]

[a] *Structural Impact Laboratory (SIMLab), Department of Structural Engineering, Norwegian University of Science and Technology (NTNU), NO-7491 Trondheim, Norway*

[b] *Centre for Advanced Structural Analysis (CASA), NTNU, NO-7491 Trondheim, Norway*

Abstract

The tensile ductility of the extruded aluminium alloy AA6063 in different tempers is investigated experimentally in this study. The results are correlated with the microstructure and the anisotropic plasticity of this alloy, previously investigated in Khadyko et al. [1]. To this end, uniaxial tensile specimens were produced from an extruded flat profile at different angles to the extrusion axis. The specimens were tested in the naturally aged (T1) condition and after heat-treatment to the peak-aged (T6), over-aged (T7) and soft annealed (O) conditions. The crystallographic texture, the precipitate content, the precipitate free zones around grain boundaries and the primary particle content were characterized prior to testing. Digital image correlation was used to measure the in-plane surface deformation and calculate strain fields during the tensile tests until fracture. The fracture surfaces were investigated in the scanning electron microscope to study the dimple structure. The tensile test results show that the tensile ductility decreases linearly with increasing tensile strength and varies markedly with the tensile direction. The tensile ductility exhibits similar directional dependency as the plastic strain ratio with some deviations around the extrusion axis, which are attributed to the anisotropy of the flow stress. The results indicate that the variation of the tensile ductility with loading direction is controlled mostly by the plastic anisotropy of the material and less by other microstructural features.

Keywords: aluminium, age hardening, ductile fracture, fracture anisotropy, plastic anisotropy, digital image correlation.

1 Introduction

The tensile strength and ductility of a 6000 series aluminium alloy are determined by its chemical composition and thermomechanical processing, which produce a broad spectrum of

microstructural features, such as constituent particles and dispersoids, solute atoms and atomic clusters, hardening precipitates of various types, and precipitate free zones around grain boundaries. The grain morphology and crystallographic texture after rolling or extrusion depend on whether the material is recrystallized or non-recrystallized. The ductile fracture process by nucleation, growth and coalescence of voids depends on these microstructural features in a complex way, which is still not fully understood. The correlation between fracture of materials given the stress and strain histories and their microstructural features has been studied in [2-4], whereas in [5, 6] fracture was observed locally on the microscale to study the underlying physical mechanisms. Experimental studies of fracture in different Al alloys resulting from various stress and strain histories are crucial for validating and improving existing damage and fracture models and for creating new ones.

Heat treatment is a common processing technique that changes the microstructure of the alloy to obtain desirable properties, such as yield strength and work-hardening capacity. The influence of heat treatment on the fracture properties of various alloys has been studied in a number of works. In these studies, an alloy is usually heat-treated to several conditions, such as solution heat-treated, peak-aged and over-aged, and then a number of mechanical tests are applied to the heat-treated specimens to obtain the fracture strain at different stress states. The AA6000 series of heat-treatable alloys was investigated in this manner in [7-13], whereas the AA2000 heat-treatable alloy series was investigated in [4, 14, 15] using a similar approach. The influence of a combination of rolling and heat treatment was studied in [16] for the AA7075 alloy. The grain boundary precipitates, as well as the precipitate free zones, that form in the peak-aged and over-aged conditions, seem to play an important role in the fracture of these heat-treatable alloys. The material's yield strength and work-hardening capacity are also crucial for fracture predictions, and they depend on the heat treatment as well.

During thermomechanical processing, such as rolling or extrusion and subsequent heat treatment, certain grain orientations may become more dominant, forming the crystallographic texture of the material. The crystallographic texture is seen as the main contributing factor to the plastic anisotropy of rolled and extruded alloys [17, 18]. Anisotropic plasticity may lead to fracture anisotropy by changing the stress state and the plastic flow of the material. The thermomechanical processing also defines the grain size and shape, the precipitate free zones around the grain boundaries, and the primary particle distribution,

which are assumed to be important contributing factors to the fracture anisotropy. Experimental studies of fracture anisotropy usually rely on a set of different specimen geometries and loadings to obtain different stress histories, and in addition the specimens are produced at different angles to the material coordinate axes. Predominantly only three directions are used: the one coinciding with the rolling or extrusion direction, the one coinciding with the width direction of the sheet, plate or profile, and the diagonal one at 45° to them both. The fracture anisotropy of the AA6000 series was studied in [19-22] and of the AA2000 series in [23-26]. Other alloy series have also been explored but to lesser extent, and some relevant articles include [27] for AA7075, [28] for AA1235 foils, [29] for AA5182, and [30] for an AA3000. In a recent article [31], the effects of the primary particle distribution on the fracture anisotropy of the 6000 series alloys were investigated.

The strains at fracture may be measured post-mortem, from the area of the fracture surface on the specimens after the tests [28, 32]. This method has many limitations and provides only information about the very final point in the fracture evolution. Alternatively, in some recent works, digital image correlation (DIC) is used to measure the strains on the surface of the specimens and the finite element method (FEM) is applied to estimate the local strains and stresses inside the material before and at fracture. The accuracy of such combined experimental-numerical methods depends largely on the accuracy and relevance of the material model. Studies on fracture anisotropy of aluminium alloys using the combined DIC-FEM approach include [20, 32-37], but the same method is broadly used also for other metals, such as Mg in [38] and steel in [39-41].

The plastic anisotropy of Al alloys is mostly attributed to crystallographic texture, but in some cases the heat treatment also plays a role, as shown in [42, 43]. The anisotropy of the tensile ductility is therefore assumed to be affected by heat treatment in a complex way, where the changing plastic anisotropy of the material interacts with the changing precipitate structure and other possible microstructural features. Few studies were dedicated to exploring these interactions. In [44], AA7075 alloy sheet material was heat-treated to underaged, peak-aged and over-aged conditions, and test specimens were produced in the rolling and width directions of the sheet. In a similar manner, AA7050 alloy sheet material was used in [45] to estimate the in-plane anisotropy of plasticity and fracture before and after heat treatment, using specimens cut in the rolling, width and diagonal directions. A complete study of such

kind would explore the fracture behaviour of the aluminium alloys as a function of heat treatment, material direction (with both in-plane and out-of-plane directions) and stress history, which would imply a large number of tests. Nevertheless, even the more limited studies, where some of these factors are held constant, are of great value.

The current study addresses the anisotropic tensile ductility of an extruded AA6063 alloy in different tempers, i.e., the interaction effects of heat treatment and plastic anisotropy on the tensile ductility are investigated. In a previous study [1], the influence of heat treatment on the plastic anisotropy was thoroughly investigated for the same material. Uniaxial tensile specimens were produced from an extruded plate at different angles to the extrusion axis and heat-treated to different tempers prior to the mechanical testing. DIC was used to track the surface deformation during the tests until necking. Crystal plasticity finite element simulations were used to estimate the effect of the crystallographic texture on the plastic anisotropy. The present study focuses in turn on the localized deformation after necking and until fracture in these specimens. DIC was used to calculate the strains after necking and to estimate the state of stress and strain at fracture in specimens with different material orientations. The experimental results indicate that plastic anisotropy is the main contributor to the variation of the tensile ductility with in-plane loading direction, whereas other microstructural features seem less important for the actual material.

2 Material characterization and experimental procedures

Direct-chill cast billets of the AA6063 alloy were produced by Hydro Aluminium. The chemical composition of the alloy is given in Table 1. The material was homogenised in the batch homogenisation furnace and extruded to flat profiles with 205 mm width and 3 mm thickness. The crystallographic texture of the material was determined from electron backscatter diffraction (EBSD) measurements. The through-thickness section used for EBSD demonstrated a strong cube texture with a minor Goss component, typical for the extruded and recrystallized alloys. The plot of the orientations measured by the EBSD on the cross-section of the profile is shown in Figure 1.

Uniaxial tensile specimens of the dog-bone type were produced from the extruded profile at 0°, 5°,10°,15°, 22.5°, 45°, 67.5° and 90° to the extrusion axis. The specimens in 5°,10° and 15° directions were used to investigate the flow stress anisotropy in Khadyko et al. [1], but

were not used in the present study. The gauge part of the specimens had 8 mm width and length of 35 mm. The specimens were then heat treated to T6 (peak-aged), T7 (over-aged) and O (soft annealed) tempers. The as-received material was stored at room temperature for a prolonged period and may be classified as T1 temper, i.e., naturally aged to a substantially stable condition. Two specimens were produced for each orientation and temper combination, giving a total of 40 specimens.

The undeformed, heat-treated material was investigated in the transmission electron microscope (TEM). The precipitate shape, size and density were found for the heat-treated material. The T6 temper showed a combination of a high density of small and a low density of larger needle-like precipitates. The T7 temper was characterized by a lower density of coarser needle-like precipitates. In addition, precipitate free zones were found along the grain boundaries in both tempers. The O temper contained a small number of large plate-like precipitate particles. Both T6 and T7 tempers contained a small number of the large plate-like particles as well. The precipitate sizes and densities calculated from the TEM images may be found in [1]. In addition, the precipitate free zones (PFZ) were identified in the T6 and T7 tempers, see Figure 2. The average width of the PFZ was estimated to 150 nm in the T6 temper and 300 nm in T7 temper. As the T1 temper contains mostly aggregated solid solution, it was excluded from the TEM study.

To investigate the primary particle content in the material, two flat samples were produced from the alloy in T1 temper in the undeformed state. One sample had its main plane normal to the transverse direction and the other normal to the extrusion direction. The study was performed using a Hitachi SU6600 scanning electron microscope at 10kV with a BSE COMP detector with working distance of 15 mm. The images were analysed with the ImageJ software. An overview of the primary particle distribution and morphology in the two specimens is presented in Figure 3. The area fraction of the primary particles is found to be 0.4 % from both samples. The average minimum feret diameter was found to be about 0.6 µm for the first sample and 0.5 µm for the second sample. The maximum feret diameter was found to be 2.5 µm for the first sample and 1.9 µm for the second sample. The two specimens have very similar primary particle distributions. Most particles are elongated along the horizontal axis of the image, i.e., along either the extrusion or the transverse direction. The typical stringer structure that form when particles break during the extrusion was not

exhibited. Considering the similarity between the samples, many particles could have platelet shape.

The tensile tests were performed at low deformation rates, and may be considered quasi-static. A speckle-pattern was painted on one of the surfaces of the specimens prior to testing, and this surface was photographed with a Prosilica GC 2450 camera at 1 Hz frequency during testing. The image size was 2448 × 2050 pixels. The in-house DIC software eCorr v4.0 [46] was used to post-process the images and calculate the displacement and strain field on the surface. The DIC mesh used to calculate the engineering stress-strain curves and the strain fields before necking consisted of 25 × 25 pixels bilinear four-node elements, with an element size of approximately 0.7 mm, corresponding to a resolution of about 0.03 mm/pixel. The noise level estimated at the start of the test was not more than 0.05 pixels, corresponding to $1.5 \cdot 10^{-4}$ mm for the displacements and $1.0 \cdot 10^{-3}$ for the strains. The engineering strains were calculated using a virtual extensometer on the DIC mesh, which covered the gauge part of the specimen.

A complete description of the methods and results of the material characterization and tensile testing is found in Khadyko et al. [1].

3 Estimating local strains at fracture

Ductile fracture in the uniaxial tensile specimens occurs typically after necking, when the stress and strain fields become heterogeneous. Therefore, measuring the fracture strain is not a trivial task. In some cases, fracture strain is calculated from the fracture surface area on the fractured specimens after the tensile test. This method may give reasonably accurate results (in an average sense) for cylindrical specimens and well-defined fracture surfaces, whereas for the planar specimens used in this work another method is required. Necking distorts the rectangular cross-section into a complex shape, which, together with the slanted irregular fracture surface, prevents accurate area measurements.

Using the DIC method, the in-plane strains on the surface of the specimen may be calculated directly, without additional assumptions about the material. The accuracy of the results is then only limited by the quality, resolution and frequency of the images.

The first issue is to identify the point of fracture initiation. When DIC is used, onset of fracture is identified by the last image before fracture. The accuracy is thus limited by the frequency of the imaging. In some studies, the onset of fracture is associated with the formation of cracks on the surface of the specimen [47]. In our case, the crack formation could not be reliably traced for most specimens, see e.g. the specimen in Figure 4 a). Instead, it was found that for all specimens, a point in the deformation history exists, at which the force drops abruptly and the displacement rate jumps. In the case of the T1 and T6 tempers, this point in time coincides with the last image before the specimen breaks into two halves. For the T7 and O tempers, the specimen continues to deform as one piece after this point in time, but its load-carrying capacity becomes virtually non-existent so this image was chosen to represent the onset of fracture.

The second issue is the choice of mesh resolution. The deformation in the neck area is highly inhomogeneous and complex, which requires a fine mesh to resolve the deformation field. On the other hand, a small element size leads to high noise levels, less accuracy and eventually convergence problems. As mentioned before, the pre-necking deformation was measured on the 25 × 25 pixels mesh, which was stable and had low noise levels, but was too coarse for the post-necking inhomogeneous deformation. After some attempts, a mesh size of 15 × 15 pixels was chosen, as a compromise, for the post-necking deformation calculations. The size of one element is thus approximately 0.5 mm. This mesh size provided sufficient convergence and allowed resolving some complex strain patterns in the necking zone.

The 15 × 15 pixels mesh is still too coarse to resolve the finest details of the deformation field in the localization zone. The final localization band, in which fracture develops, is so narrow that the strains calculated in the DIC elements depend somewhat on the exact position of the nodes of the mesh. The node may lie close to the middle of the band. In this case the two elements adjacent to the node have similarly high strain levels. In other cases, the band lies between two nodes and the element built on these nodes obtains the highest strain level, with lower strains in the adjacent elements. Correspondingly, the average strains in the band, calculated from these two meshes, may differ. To remove the influence of the mesh position, the DIC analysis was run 7 times, with 7 identical meshes, positioned with a 2 pixel offset from each other for every run. In this way, many possible resolutions of the localization band

were obtained and the average deformation and strain fields were calculated, independent of the mesh position.

To reduce the influence of noise and obtain a more objective measure of strains, the deformation gradient averaging procedure, described in Khadyko et al. [1], was used. The elements used in the averaging were chosen as follows. The deformed mesh at the onset of fracture was obtained. The contour plot of the logarithmic strain in the tensile direction was then obtained as shown in Figure 4 b). The range of the contour plot was modified by a cut-off limit to find the localization band in the deformed mesh, which could be from two to four elements wide. The elements on the upper and lower ends of the band were excluded from consideration, as well as the occasional outlying elements on the side of the band. The resulting example of the element set used for the deformation gradient averaging is also shown in Figure 4 c). The average deformation gradient tensor was used to calculate the Cauchy-Green deformation tensor. Then the eigenvalues and eigenvectors of the Cauchy-Green deformation tensor were used to find the logarithmic strain tensor in the principal axes of deformation, which was subsequently rotated to the coordinate system based on the tensile axis of the specimen. The procedure was performed several times with offset mesh positions, as described previously. The resulting average surface strain over the localization band at the onset of fracture is in the following called the fracture strain and denoted $\bar{\varepsilon}_f$.

4 Results

4.1 Stress-strain behaviour

The influence of heat treatment on yield strength, work-hardening and plastic anisotropy was discussed in detail in Khadyko et al. [1]. Two diagrams from [1] that are most relevant for the present study are the strain ratio q and the flow stress ratio $\sigma_\varphi / \sigma_{90}$ plotted against the tensile direction $\varphi \in [0°, 90°]$. These diagrams are reproduced in Figure 5. The strain ratio was defined as $q = -d\varepsilon_y / d\varepsilon_x$, where ε_x and ε_y are the logarithmic strains in the tensile direction and the width direction of the specimen, respectively. In the definition of the flow stress ratio, σ_φ and σ_{90} are the true stresses in material directions φ and 90°, respectively, at given values of specific plastic work. Thus, the 90° direction is taken as a reference direction for the material. The strain ratio q expresses the plastic flow anisotropy of the material, whereas the

flow stress ratio $\sigma_\varphi / \sigma_{90}$ signifies the strength anisotropy. Figure 5a shows that q varies with tensile direction, signifying anisotropy in plastic flow, and has a local maximum at φ equal to $0°$, a global minimum for φ in the range between $22.5°$ and $45°$ depending on the temper, and a global maximum at φ equal to $90°$. Except for the tests at $45°$, there is little variation in q with temper. Note that a low value of q implies a stronger tendency for thinning of the tensile specimen, whereas a value close to unity signifies a higher resistance against thinning. Figure 5b demonstrates that $\sigma_\varphi / \sigma_{90}$ is fairly independent of temper for φ in the range between $22.5°$ and $90°$, whereas for lower values of φ, there are significant differences, which have been discussed in more detail in [1]. However, it is noted that $\sigma_\varphi / \sigma_{90}$ lies between 0.94 and 1.06 for all tensile tests. Thus, the variation with tensile direction and temper is rather limited, indicating moderate strength anisotropy compared with the plastic flow anisotropy.

The engineering stress-strain curves until fracture from the tensile experiments are presented in Figure 6. The plots show the strong variations in the strength, work-hardening and post-necking behaviour due to the heat treatment. The deviation between the two test repetitions is negligible before necking, but becomes higher after necking sets in. A part of this deviation could be attributed to measurement error. Often the neck was not situated in the middle of the gauge area, but close to the edge, and, consequently, the position of the virtual extensometer over the neck may have affected the measured strains. The other possibility is minor deviations in the material behaviour itself, as the unstable post-necking behaviour is very sensitive to imperfections. Nevertheless, the deviations are moderate enough to not completely obscure the trends that heat treatment and material anisotropy introduce into fracture. After necking, the engineering stress starts to drop at an increasing rate. The engineering strain interval between necking and fracture is usually quite short. The T7 temper stands out in this regard. For this temper, the strain interval between necking and fracture is larger than the interval between yielding and necking. The anisotropy of the global engineering fracture strain for different tempers is markedly different. The only common trend is that it is typically smallest for the specimens in the 0° direction for all tempers considered.

4.2 Strain distributions within the neck region

The next step is to analyse the local deformation in the neck area. Some typical results of the DIC calculations on a mesh of 15 × 15 pixels elements are presented in Figure 7. The logarithmic tensile strain field in the neck area at fracture is plotted for two orientations with the extreme values of the strain ratio, namely 45° and 90°, as well as the 0° direction, which is most often the least ductile orientation. The neck width and strain concentration depend primarily on the heat treatment. The T6 specimens have characteristically a wide neck without a well-defined strain concentration band, which the other tempers possess. The material orientation influences the necking process as well. In the 45° direction, the neck is inclined for all tempers due to the crystallographic texture effect. It may also be observed that the neck in the 90° specimens is wider than in the 0° specimens, likely due to the larger value of the strain ratio q.

The distribution of the logarithmic tensile strain along the gauge length of a 90° specimen for all tempers is shown in Figure 8. The strain at each point is the average strain of a row of DIC elements with the same tensile axis coordinate. This plot demonstrates some particular trends in the homogeneous strain (i.e., the strain before necking) and the strain close to fracture. The O temper is a soft and ductile temper having both the highest homogeneous strain and fracture strain. Temper T1 has relatively high homogeneous strain, but low fracture strain, while for temper T7 the contrast is the strongest, with the lowest homogeneous strain and a high fracture strain, reaching 100%.

The average in-plane logarithmic strains in the neck area were calculated, using the method described in Section 3, and plotted as the negative transverse strain $\bar{\varepsilon}_y$ versus the longitudinal strain $\bar{\varepsilon}_x$ in Figure 9. The superposed bar signifies that the strain component is averaged over the neck region. Thus, the slope of the curves equals the strain ratio q. The results for the two repeat tests are consistent, with the largest deviation for the T6 temper. In all cases, the strain state after necking is approaching a plane-strain tension state, with q decreasing visibly. This may be explained by the flat shape of the specimen, which creates a constraint in the width direction. At higher strain the material in the centre of the specimen can only preserve its volume by contracting in the thickness direction. This observation has implications for the fracture process as well. The stress state in plane-strain tension is different from uniaxial

tension in that the stress triaxiality is higher and the magnitude of the Lode parameter is lower.

4.3 Average stress-strain curves

Knowing the average in-plane strains in the neck allows estimating the average stress in the specimen after necking based on the measured force and the current section area, provided plastic incompressibility, small elastic strains and uniform strain fields thorough the thickness are assumed. The stress $\bar{\sigma}$ is defined as the force divided by the current section area, which is calculated from the average surface strains. The results are presented in Figure 10. To improve the readability of the plot, the stress-strain curves for the different tensile directions are plotted with a 100 MPa offset from one another. The results for the repeat tests are consistent until large strains close to the onset of fracture. Compared to the engineering stress-strain curves in Figure 6, the slopes of the stress-strain curves from tests in different tensile directions are similar. The variations in the work-hardening rate typical for the pre-necking deformation seem to diminish further in the deformation history. However, it is important to keep in mind that the calculated stress-strain curves include the hydrostatic stress contribution and are therefore different from the equivalent stress-strain curve after diffuse necking (see e.g. [48]).

4.4 Average fracture strains

To address the fracture anisotropy, the average logarithmic strains in the neck area at onset of fracture, as defined in Section 3, are presented in Figure 11 as function of the tensile direction. All tempers have minimum tensile ductility at φ equal to 45° and maximum at φ equal to 90°. Tempers T1 and T6 have a local minimum at the 0° orientation, whereas tempers T7 and O have a local maximum at this orientation. The difference between the minimum and the maximum fracture strain for the same temper is from around 15% for the T1, T6 and T7 tempers to 20% for the O temper. The average strain at onset of fracture is also plotted against the average stress at necking in Figure 12. The average stress at necking was chosen as a more reliable and accurate stress estimate than average stress at onset of fracture, which is uncertain due to the assumptions and limitations of the DIC calculations. The trend in this plot is a reverse proportionality, where a high stress level corresponds to a low fracture strain and vice versa. Figure 13 shows the same measure of the fracture strain as a function of the strain ratio q. To make the trends more clear, a trend line is fitted to the data for each temper. While the

data is noisy, the generally larger strain ratio and fracture strain at 90° and smaller strain ratio and fracture strain at 45°, with other directions lying in-between, indicate that the tensile ductility increases with increasing strain ratio and thus with higher resistance to thinning of the specimen. A similar observation was made in Fourmeau et al. [49].

4.5 Fracture surfaces

The fracture surfaces of the specimens were studied in the Scanning Electron Microscope (SEM). For each temper, one tensile specimen was selected for each of the 0°, 45° and 90° loading directions. The fracture surface of a specimen in a given tensile direction has a distinct cross-section shape that is a result of the material's plastic anisotropy. The intensity of the cross-section distortion varies with the heat treatment, but the shape remains clearly identifiable and similar for all tempers. The O temper was thus used to illustrate the trends.

SEM images of the O temper specimens are presented in Figure 14. The cross-section of the 0° specimen is more compressed in the thickness direction (reflecting the strain ratio $q < 0.5$) with concave edges bowing towards the centre of the specimen. The cross-section of the 45° specimen is even thinner (corresponding to an even lower value of the strain ratio q) with almost straight horizontal edges and convex vertical edges, bowing away from the centre. The cross-section of the 90° specimen has concave edges again. The proportion between the width and thickness of the fracture surface is determined largely by the strain ratio q, which in this case is greater than 0.5. The cross-section is correspondingly less compressed in the thickness direction than in the width direction.

The high magnification SEM images of the fracture surfaces show the features typical for a ductile fracture. The expanded and coalesced voids left dimples of various sizes, sometimes with a particle visible in the centre. The images obtained for the different material orientations hardly show any distinct features, therefore they are not presented. The differences between the specimens with different heat treatments are much more significant. The images taken with 1000 times magnification at the centre of the 0° specimen for all four tempers are shown in Figure 15. The most ductile O temper shows the largest dimples, while the dimple size for the T1, T6 and T7 tempers is similar. Though, tempers T6 and T7 show shallower dimples than temper T1. In addition, tempers T6 and T7 demonstrate some flat areas, where the grains separated along the grain boundaries, most likely in the precipitate free zones. The similarity

between fracture surfaces of the T6 and T7 tempers is remarkable, considering how different their fracture strains are.

5 Discussion

The results presented in the previous section are obtained from DIC calculations on a mesh that is a compromise between accurately describing the local deformation on the surface of a specimen and obtaining a numerically stable and accurate solution of the DIC calculations. Therefore, the calculated strain fields have limited resolution and a substantial level of noise in addition to the intrinsic inhomogeneity of the deformation in the real material. Improving the accuracy in this case is limited by the quality and resolution of the available images and the implemented DIC algorithms. To address this issue, most of the results presented in this study are obtained by averaging the behaviour of multiple elements, demonstrating similar deformation patterns. While the noise is hard to ignore on the level of individual elements and smaller groups of elements (see Figure 7 and Figure 8), the average results exhibit much less noise and more consistent behaviour.

The out-of-plane deformation of the specimen may affect the accuracy of the in-plane strain calculations, but this effect is most likely very small for the used camera and distance to the specimen [50]. Another issue is the use of surface displacements to assess the behaviour of a specimen. Before necking the deformation is mostly homogeneous through the specimen thickness, but the localization leads to a progressively more inhomogeneous strain field. Surface strain is just one facet of this process, but it is the only one that can be reliably measured throughout the test with the adopted experimental set-up. Even keeping in mind all the aforementioned limitations and assumptions, the results obtained for different tempers and orientations show some clear qualitative trends. The repeat tests also show good consistency with each other.

One way to bypass some of the limitations of the DIC method is to use the measured surface displacements and the tensile force as the input into a finite element model, which may then produce the local strain fields with higher resolution. In this study, the materials demonstrate quite complex behaviour in several aspects, but first and foremost it is plastically anisotropic. Some type of anisotropic yield surface may in principle be calibrated using the experimental data, but this data only covers part of the yield surface which describes uniaxial tension. The

strain analysis on the other hand shows that the stress state is closer to plane-strain tension at fracture. Another method used to calibrate the yield surface of anisotropic metals is polycrystal plasticity simulations and texture data [48]. In Khadyko et al. [1], it was shown that the polycrystal plasticity simulations only predict the behaviour of the material in a qualitative sense, partly due to the variations in the anisotropy caused by the heat treatment. The texture evolution at large strains will further lead to distortional hardening, which is very hard to describe by phenomenological plasticity models. Using a polycrystal plasticity based yield surface to obtain some quantitative predictions of the tensile behaviour would inevitably introduce an additional significant source of error.

The heat treatment affects mostly the solid solution and precipitate contents in the material. It has a strong effect on the yield stress and the work-hardening, due to the change in the amount of dislocation obstacles. In the T6 and T7 tempers, it also creates PFZs of different widths and large grain-boundary precipitates (see Figure 2). The crystallographic texture is unaffected by the type of heat treatment used in this study. Another microstructural feature that is left unaltered is the primary particles. From a mechanical point of view, the chief effect of the heat treatment is on the stress levels in the specimen. The strong linear trend that may be seen in Figure 12 connects the stress levels and the tensile ductility. The T6 and T1 tempers have very similar stress levels at necking, but very different work-hardening rates, precipitate content and PFZs (which are absent from the T1 temper). Although temper T1 has slightly higher fracture strains than temper T6, it is a second-order effect on this diagram, despite their fundamental microstructural dissimilarity.

The combination of cube and Goss texture in the extruded plate produced a particular type of plastic anisotropy. On the one hand, as shown in [1], the flow stress anisotropy is not strong, with 10% difference in flow stress between different material directions. In many studies, only two directions are used, namely the 0° and 90° directions. The difference in yield stress and ultimate stress between these two directions is very small for the O temper, and based on the flow stress ratio alone, one would be led to the conclusion that the material is only slightly anisotropic. On the other hand, the plastic flow anisotropy, as demonstrated by the strain ratio, is strong, with the 90° orientation having a markedly different strain ratio than the 45° orientation. By comparing the plot of fracture strain against tensile direction to the plots of flow stress ratio and strain ratio against tensile direction, some remarkable trends become

evident. Regardless of the temper, the 90° direction gives the maximum value of the strain ratio and the fracture strain, and at the 45° direction both these measures reach their minimum value. The 67.5° and 22.5° directions lie somewhere between the two extremes, whereas the 0° direction demonstrates a complex behaviour. For T1 and T6 tempers, it has a higher flow stress ratio than the T7 and O tempers, while the difference in the strain ratio is not significant, as may be seen in Figure 5. This is accompanied by a noticeably lower fracture strain in the 0° direction for the T1 and T6 tempers. The connection between the strain ratio and the fracture strain is further illustrated in Figure 13. Even for the T1 and T6 tempers, the general trend is still the same: a low/high value of the strain ratio goes together with a low/high value of the fracture strain. These observations may be compared to the results described in [51], where a connection between the strain ratio and the fracture strain, similar to the one observed in this work, was found for a 7000 series aluminium alloy. In that work, a localization approach was proposed that associates ductile fracture with a material instability.

The primary particles in the extruded material may contribute to the so-called topological anisotropy. The extrusion process breaks and aligns the primary particles in stringers along the extrusion direction, which facilitates fracture in the transverse direction. In the present study, however, the primary particles do not form stringers and do not show much in-plane anisotropy, at least not in the studied 0° and 90° directions. Therefore they seem to have no effect on the fracture anisotropy of the material.

6 Conclusions

The experimental study on the tensile ductility of the extruded aluminium alloy AA6063 in tempers T1, T6, T7 and O shows that the alloy exhibits a fracture anisotropy that is chiefly independent of the heat treatment and governed mainly by the plastic anisotropy of the alloy introduced by the extrusion process and the subsequent recrystallization. The fracture strain is greatest in the transverse (90°) direction and least in the 45° direction of the extruded profile for all tempers. The heat-treatment changes the global ductility by changing the yield and tensile strengths of the material. The fracture strain tends to decrease with increasing tensile strength and this scaling relationship is approximately linear, as also found in previous studies. As a result, the soft O temper exhibits the highest ductility, followed in turn by the T7 and T1 tempers, whereas the peak-aged T6 temper demonstrates the lowest ductility. Fractography showed that the fracture process was ductile for all tempers and in all tensile

directions. The fracture surfaces exhibited dimples of various sizes, depending on the yield strength and work-hardening of the actual temper. Some intergranular fracture was observed for the T6 and T7 tempers and attributed to the precipitate free zone along the grain boundaries in these tempers.

Acknowledgements

The authors gratefully appreciate the financial support from NTNU and the Research Council of Norway through the FRINATEK Programme, Project No. 250553 (FractAl). Fractography SEM images courtesy of S. Thomesen.

References

[1] M. Khadyko, C. Marioara, S. Dumoulin, T. Børvik, and O. S. Hopperstad, "Effects of heat-treatment on the plastic anisotropy of extruded aluminium alloy AA6063," *Materials Science and Engineering: A,* 2017.

[2] K. O. Pedersen, T. Børvik, and O. S. Hopperstad, "Fracture mechanisms of aluminium alloy AA7075-T651 under various loading conditions," *Materials & Design,* vol. 32, no. 1, pp. 97-107, 2011.

[3] B. Decreus, A. Deschamps, P. Donnadieu, and J. Ehrström, "On the role of microstructure in governing fracture behavior of an aluminum–copper–lithium alloy," *Materials Science and Engineering: A,* vol. 586, pp. 418-427, 2013.

[4] M. Fourmeau, C. Marioara, T. Børvik, A. Benallal, and O. S. Hopperstad, "A study of the influence of precipitate-free zones on the strain localization and failure of the aluminium alloy AA7075-T651," *Philosophical Magazine,* no. ahead-of-print, pp. 1-27, 2015.

[5] T. F. Morgeneyer *et al.*, "In situ 3-D observation of early strain localization during failure of thin Al alloy (2198) sheet," *Acta Materialia,* vol. 69, pp. 78-91, 2014.

[6] A. Buljac, T. Taillandier-Thomas, T. F. Morgeneyer, L. Helfen, S. Roux, and F. Hild, "In situ observation of strained bands and ductile damage in thin AA2139-T3 alloy sheets," *Procedia IUTAM,* vol. 20, pp. 66-72, 2017.

[7] A. Asserin–Lebert, J. Besson, and A.-F. Gourgues, "Fracture of 6056 aluminum sheet materials: effect of specimen thickness and hardening behavior on strain localization and toughness," *Materials Science and Engineering: A,* vol. 395, no. 1, pp. 186-194, 2005.

[8] T. Furu and K. Pedersen, "The influence of grain structure and texture on formability and toughness of extruded aluminium alloys," in *Materials Science Forum*, 2006, vol. 519, pp. 1421-1428: Trans Tech Publ.

[9] T. Morgeneyer, M. Starink, S. Wang, and I. Sinclair, "Quench sensitivity of toughness in an Al alloy: Direct observation and analysis of failure initiation at the precipitate-free zone," *Acta Materialia,* vol. 56, no. 12, pp. 2872-2884, 2008.

[10] A. Simar, K. L. Nielsen, B. de Meester, V. Tvergaard, and T. Pardoen, "Micro-mechanical modelling of ductile failure in 6005A aluminium using a physics based strain hardening law including stage IV," *Engineering Fracture Mechanics,* vol. 77, no. 13, pp. 2491-2503, 2010.

[11] I. Westermann, K. O. Pedersen, T. Furu, T. Børvik, and O. S. Hopperstad, "Effects of particles and solutes on strength, work-hardening and ductile fracture of aluminium alloys," *Mechanics of Materials,* vol. 79, pp. 58-72, 2014.

[12] K. O. Pedersen, I. Westermann, T. Furu, T. Børvik, and O. S. Hopperstad, "Influence of microstructure on work-hardening and ductile fracture of aluminium alloys," *Materials & Design,* vol. 70, pp. 31-44, 2014.

[13] I. Westermann, K. O. Pedersen, T. Børvik, and O. S. Hopperstad, "Work-hardening and ductility of artificially aged AA6060 aluminium alloy," *Mechanics of Materials,* vol. 97, pp. 100-117, 2016.

[14] H. Li *et al.*, "Effect of Double Aging on the Toughness and Precipitation Behavior of a Novel Aluminum-Lithium Alloy," *Journal of Materials Engineering and Performance,* vol. 24, no. 10, pp. 3912-3918, 2015.

[15] N. D. Alexopoulos, A. Proiou, T. Examilioti, N. Kashaev, S. Riekehr, and S. K. Kourkoulis, "Effect of artificial aging on the mechanical performance of (Al-Cu) 2024 and (Al-Cu-Li) 2198 aluminum alloys," *Procedia Structural Integrity,* vol. 2, pp. 3782-3783, 2016.

[16] P. Das, R. Jayaganthan, and I. Singh, "Tensile and impact-toughness behaviour of cryorolled Al 7075 alloy," *Materials & Design,* vol. 32, no. 3, pp. 1298-1305, 2011.

[17] S. Li, O. Engler, and P. Van Houtte, "Plastic anisotropy and texture evolution during tensile testing of extruded aluminium profiles," *Modelling and Simulation in Materials Science and Engineering,* vol. 13, no. 5, pp. 783-795, 2005.

[18] S. Dumoulin, O. Engler, O. S. Hopperstad, and O. G. Lademo, "Description of plastic anisotropy in AA6063-T6 using the crystal plasticity finite element method," *Modelling and Simulation in Materials Science and Engineering,* vol. 20, no. 5, p. 055008, 2012.

[19] Y. Hammi, M. F. Horstemeyer, and D. J. Bammann, "An anisotropic damage model for ductile metals," *International Journal of Damage Mechanics,* vol. 12, no. 3, pp. 245-262, 2003.

[20] M. Luo, T. Wierzbicki, and D. Mohr, "Anisotropic ductile fracture of AA6260-T6 Al-alloy extrusions," in *Proceedings of the ASME International Mechanical Engineering Congress and Exposition (IMECE2011),* 2011.

[21] M. Luo, M. Dunand, and D. Mohr, "Experiments and modeling of anisotropic aluminum extrusions under multi-axial loading–Part II: Ductile fracture," *International Journal of Plasticity,* vol. 32, pp. 36-58, 2012.

[22] G. Gu and D. Mohr, "Anisotropic Hosford–Coulomb fracture initiation model: Theory and application," *Engineering Fracture Mechanics,* vol. 147, pp. 480-497, 2015.

[23] F. Bron and J. Besson, "Simulation of the ductile tearing for two grades of 2024 aluminum alloy thin sheets," *Engineering Fracture Mechanics,* vol. 73, no. 11, pp. 1531-1552, 2006.

[24] D. Steglich, W. Brocks, J. Heerens, and T. Pardoen, "Anisotropic ductile fracture of Al 2024 alloys," *Engineering Fracture Mechanics,* vol. 75, no. 12, pp. 3692-3706, 2008.

[25] T. F. Morgeneyer, J. Besson, H. Proudhon, M. Starink, and I. Sinclair, "Experimental and numerical analysis of toughness anisotropy in AA2139 Al-alloy sheet," *Acta Materialia*, vol. 57, no. 13, pp. 3902-3915, 2009.

[26] M. Janbakhsh, F. Djavanroodi, and M. Riahi, "A comparative study on determination of forming limit diagrams for industrial aluminium sheet alloys considering combined effect of strain path, anisotropy and yield locus," *The Journal of Strain Analysis for Engineering Design*, vol. 47, no. 6, pp. 350-361, 2012.

[27] M. Fourmeau, T. Børvik, A. Benallal, and O. S. Hopperstad, "Anisotropic failure modes of high-strength aluminium alloy under various stress states," *International Journal of Plasticity*, vol. 48, pp. 34-53, 2013.

[28] C. Bonatti and D. Mohr, "Anisotropic viscoplasticity and fracture of fine grained metallic aluminum foil used in Li-ion batteries," *Materials Science and Engineering: A*, vol. 654, pp. 329-343, 2016.

[29] M. Brunet, F. Morestin, and H. Walter-Leberre, "Failure analysis of anisotropic sheet-metals using a non-local plastic damage model," *Journal of Materials Processing Technology*, vol. 170, no. 1, pp. 457-470, 2005.

[30] N. Lee, J. Chen, P.-W. Kao, L. Chang, T. Tseng, and J. Su, "Anisotropic tensile ductility of cold-rolled and annealed aluminum alloy sheet and the beneficial effect of post-anneal rolling," *Scripta Materialia*, vol. 60, no. 5, pp. 340-343, 2009.

[31] F. Hannard, A. Simar, E. Maire, and T. Pardoen, "Quantitative assessment of the impact of second phase particle arrangement on damage and fracture anisotropy," *Acta materialia*, vol. 148, pp. 456-466, 2018.

[32] A. M. Beese, M. Luo, Y. Li, Y. Bai, and T. Wierzbicki, "Partially coupled anisotropic fracture model for aluminum sheets," *Engineering Fracture Mechanics*, vol. 77, no. 7, pp. 1128-1152, 2010.

[33] C. Chen, N. Liang, F. Liu, and Q. Fu, "A physical mechanism based investigation on the elasto-plastic-damage behavior of anisotropic aluminum alloys under finite deformation," *Science China Physics, Mechanics and Astronomy*, vol. 57, no. 3, pp. 400-410, 2014.

[34] G. Rousselier and M. Luo, "A fully coupled void damage and Mohr–Coulomb based ductile fracture model in the framework of a Reduced Texture Methodology," *International Journal of Plasticity*, vol. 55, pp. 1-24, 2014.

[35] Y. S. Lou and J. W. Yoon, "Anisotropic behavior in plasticity and ductile fracture of an aluminum alloy," *Key Engineering Materials*, vol. 651, p. 163, 2015.

[36] J. Cao, F. Li, X. Ma, and Z. Sun, "Study of fracture behavior for anisotropic 7050-T7451 high-strength aluminum alloy plate," *International Journal of Mechanical Sciences*, 2017.

[37] Y. Lou and J. W. Yoon, "Anisotropic ductile fracture criterion based on linear transformation," *International Journal of Plasticity*, vol. 93, pp. 3-25, 2017.

[38] Y. Jia and Y. Bai, "Ductile fracture prediction for metal sheets using all-strain-based anisotropic eMMC model," *International Journal of Mechanical Sciences*, vol. 115, pp. 516-531, 2016.

[39] G. Gruben, E. Fagerholt, O. S. Hopperstad, and T. Børvik, "Fracture characteristics of a cold-rolled dual-phase steel," *European Journal of Mechanics-A/Solids*, vol. 30, no. 3, pp. 204-218, 2011.

[40] K. Charoensuk, S. Panich, and V. Uthaisangsuk, "Damage initiation and fracture loci for advanced high strength steel sheets taking into account anisotropic behaviour," *Journal of Materials Processing Technology*, 2017.

[41] L. Dong, S. Li, and J. He, "Ductile Fracture Initiation of Anisotropic Metal Sheets," *Journal of Materials Engineering and Performance*, vol. 26, no. 7, pp. 3285-3298, 2017.
[42] N. Anjabin, A. Karimi Taheri, and H. Kim, "Crystal plasticity modeling of the effect of precipitate states on the work hardening and plastic anisotropy in an Al–Mg–Si alloy," *Computational Materials Science*, vol. 83, pp. 78-85, 2014.
[43] Z. L. Zhao, Z. Chen, and L. Liu, "The Effect of Precipitates on Anisotropy of Al-Li Alloys 2090 and 2090+ Ce," in *Advanced Materials Research*, 2010, vol. 97, pp. 496-499: Trans Tech Publ.
[44] D. Dumont, A. Deschamps, and Y. Brechet, "On the relationship between microstructure, strength and toughness in AA7050 aluminum alloy," *Materials Science and Engineering: A*, vol. 356, no. 1, pp. 326-336, 2003.
[45] H. Hu and X. Wang, "Effect of Heat Treatment on the In-Plane Anisotropy of As-Rolled 7050 Aluminum Alloy," *Metals*, vol. 6, no. 4, p. 79, 2016.
[46] E. Fagerholt. (2017). *Ecorr v.4.0 documentation*. Available: https://www.ntnu.edu/kt/ecorr
[47] M. Luo and T. Wierzbicki, "Ductile fracture calibration and validation of anisotropic aluminum sheets," in *Proceedings of 2009 SEM Annual Conference and Exposition on Experimental and Applied Mechanics, Albuquerque, NM*, 2009, pp. 402-413.
[48] M. Khadyko, S. Dumoulin, T. Børvik, and O. S. Hopperstad, "An experimental-numerical method to determine the work-hardening of anisotropic ductile materials at large strains," *International Journal of Mechanical Sciences*, vol. 88, pp. 25-36, 2014.
[49] M. Fourmeau, T. Børvik, A. Benallal, O. G. Lademo, and O. S. Hopperstad, "On the plastic anisotropy of an aluminium alloy and its influence on constrained multiaxial flow," *International Journal of Plasticity*, vol. 27, no. 12, pp. 2005-2025, 2011.
[50] E. Fagerholt, E. Østby, T. Børvik, and O. S. Hopperstad, "Investigation of fracture in small-scale SENT tests of a welded X80 pipeline steel using Digital Image Correlation with node splitting," *Engineering Fracture Mechanics*, vol. 96, pp. 276-293, 2012.
[51] D. Morin, M. Fourmeau, T. Børvik, A. Benallal, and O. S. Hopperstad, "Anisotropic tensile failure of metals by the strain localization theory: An application to a high-strength aluminium alloy," *European Journal of Mechanics-A/Solids*, vol. 69, pp. 99-112, 2018.

Tables

Table 1: Chemical composition of the AA6063 alloy.

Element	Fe	Si	Mg	Mn	Ca	Cr	Cu	Ga	Na	Ti	Zn
wt. %	0.19	0.44	0.46	0.03	0.0003	0.002	0.006	0.01	0.0003	0.01	0.008

Figures

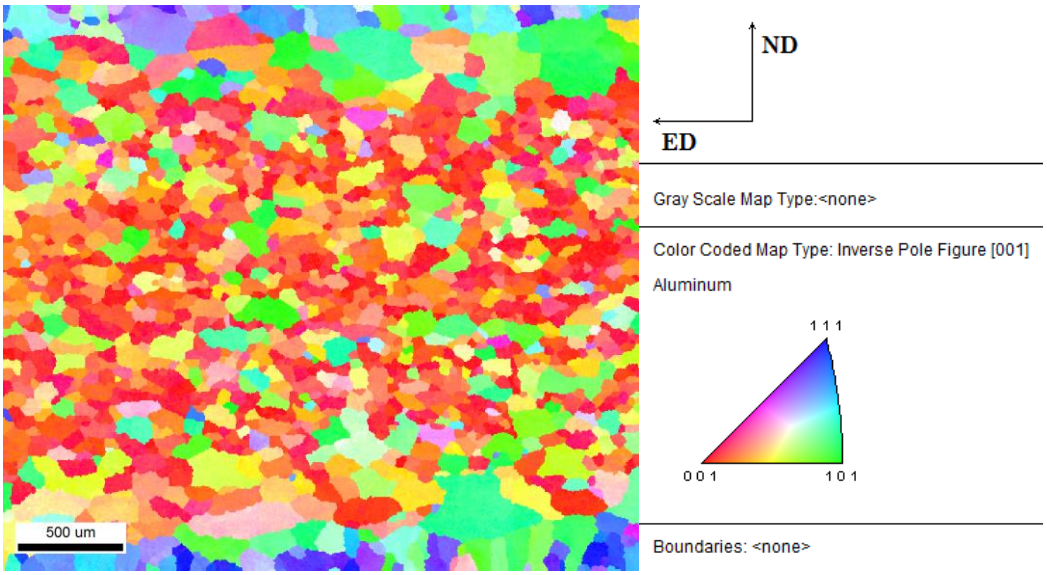

Figure 1: EBSD scan of a through-thickness cross-section of the AA6063 extruded profile. Taken from [1].

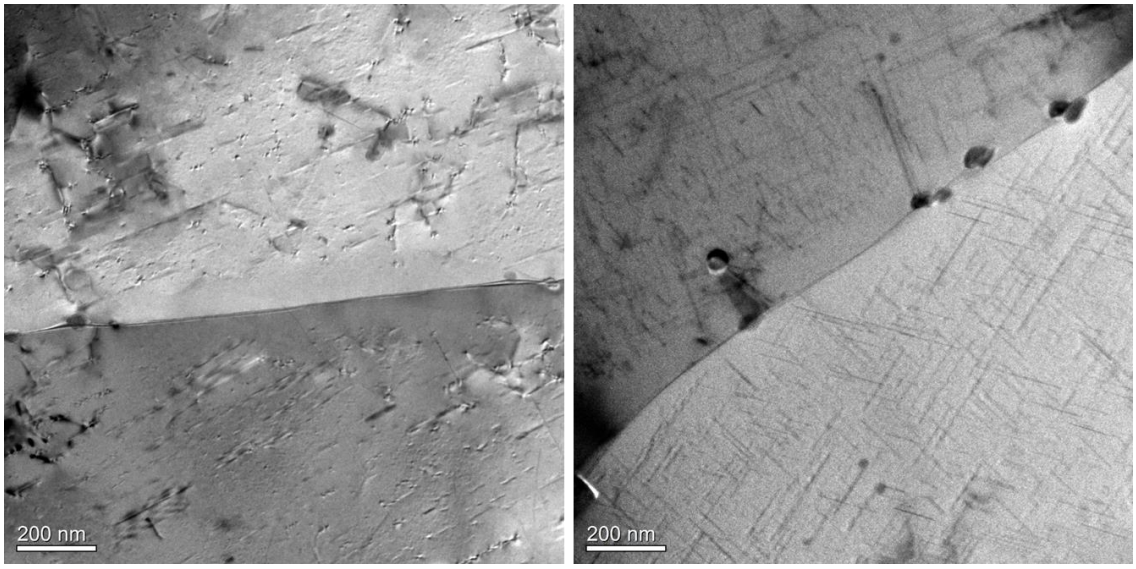

(a)

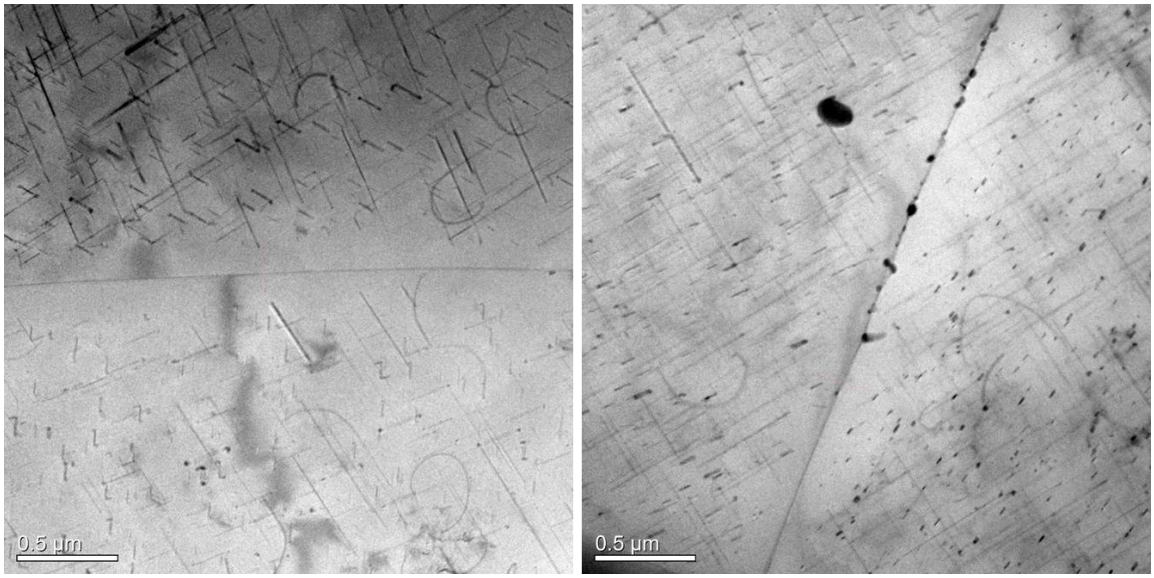

(b)

Figure 2: TEM images of the PFZ in the a) T6 temper and b) T7 temper. The right figures show the grain boundary precipitates formed inside the PFZ.

635

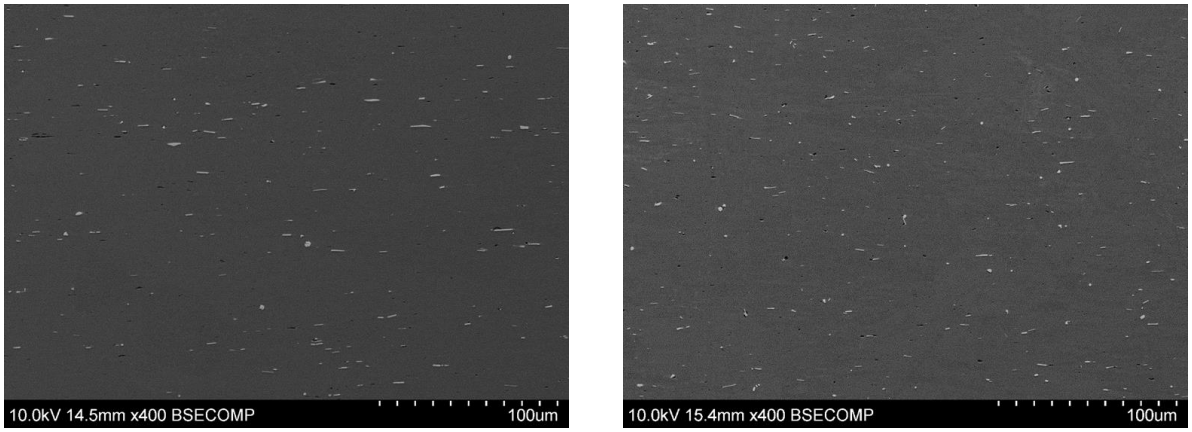

(a) (b)

Figure 3: SEM images of the primary particles in the plane normal to the a) transverse direction and b) extrusion direction of the profile. The thickness direction of the profile is in the vertical direction of the image.

640

645

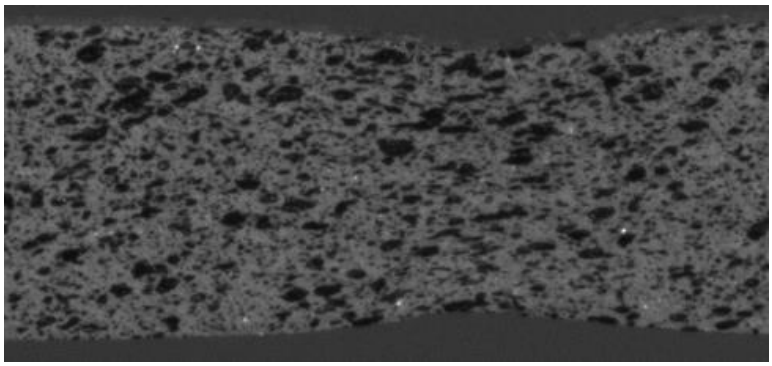

(a)

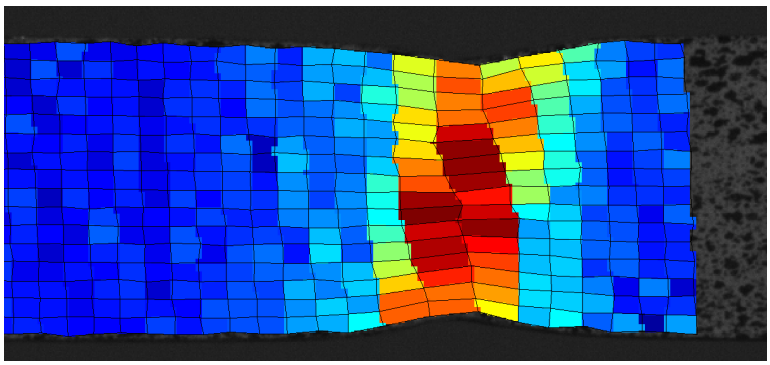

(b)

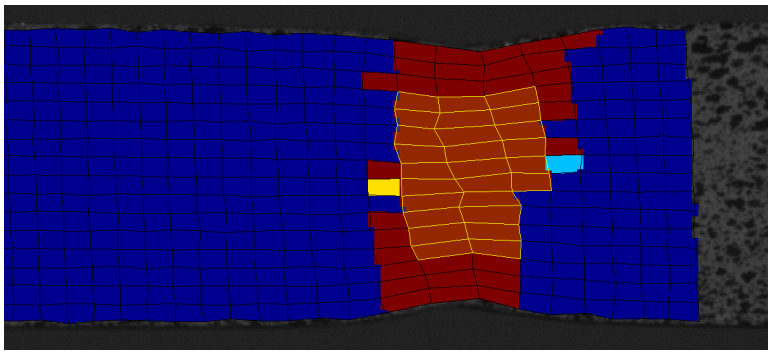

(c)

Figure 4: Necking of a specimen in T1 temper: (a) Last image of the neck area before fracture, (b) plot of logarithmic tensile strain field on the surface of the specimen at the onset of fracture, and (c) the same plot showing only the elements with strain levels exceeding the cut-off limit and the elements chosen for the averaging procedure.

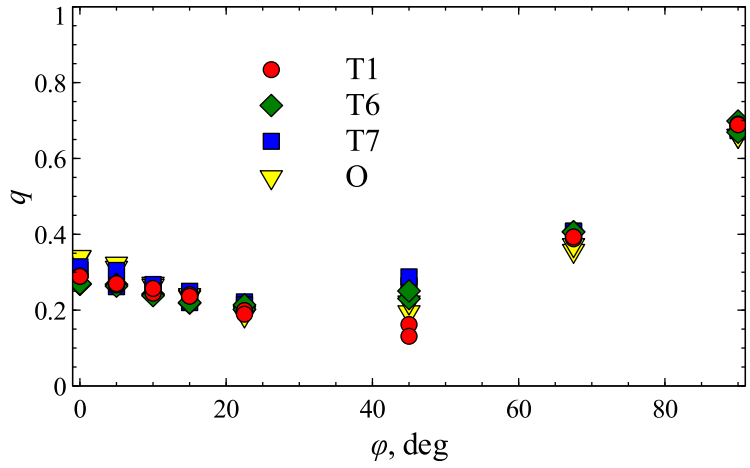

(a)

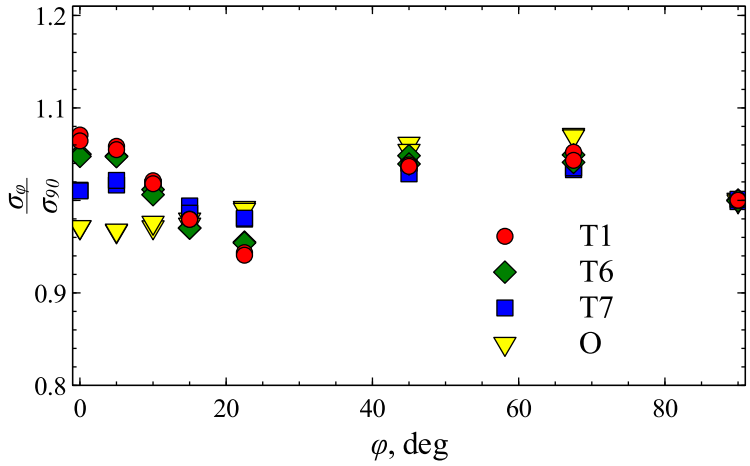

(b)

Figure 5: (a) Strain ratio, q, and (b) flow stress ratio, $\sigma_\varphi / \sigma_{90}$, as a function of the specimen orientation, φ, for all tempers at 5% logarithmic tensile strain. Taken from [1].

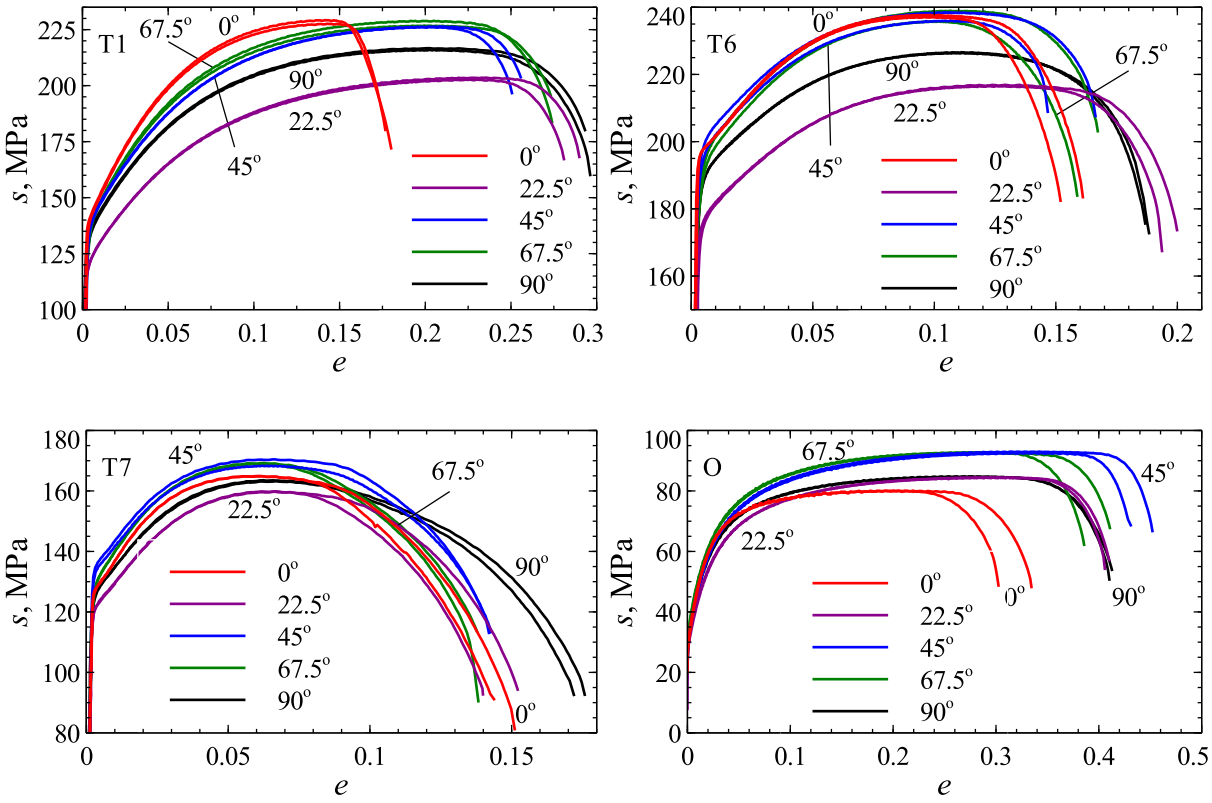

Figure 6: Engineering stress, s, vs. engineering strain, e, curves obtained for different material directions and plotted until fracture.

665

670

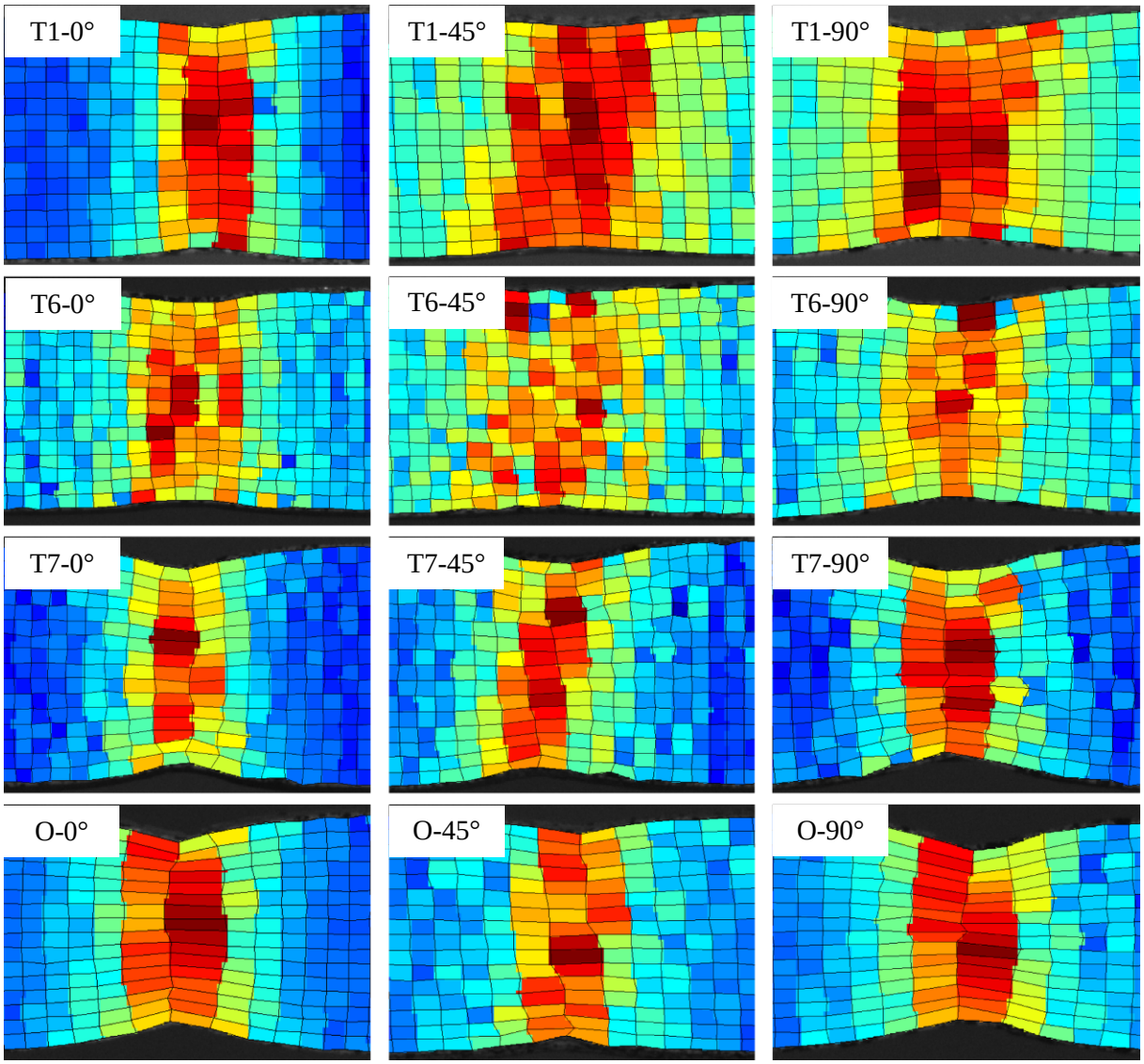

Figure 7: Field map of the logarithmic strain in the tensile direction on the DIC mesh at fracture within the neck area. The ranges of strain magnitude for the plots may be assessed from Figure 8.

675

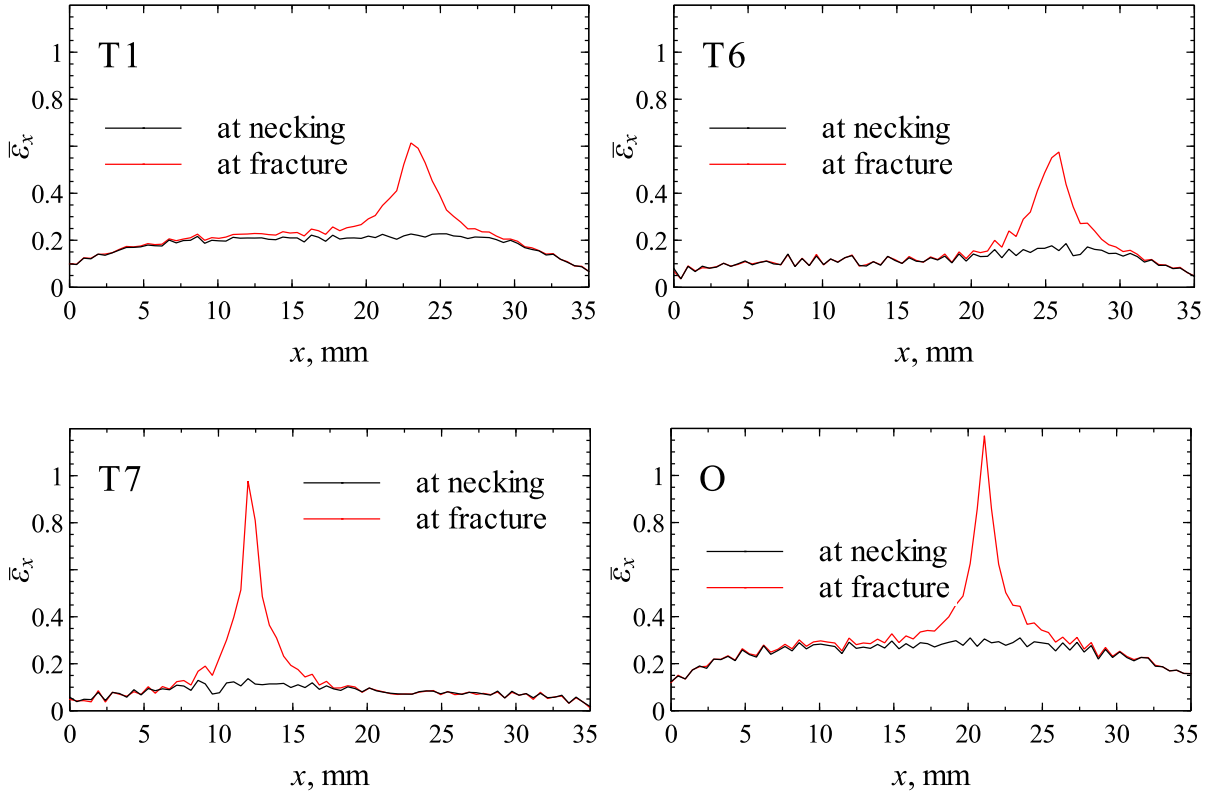

Figure 8: Profiles of the average logarithmic tensile strain, $\bar{\varepsilon}_x$, in the 90° direction specimens along the length coordinate, x, of the specimen gauge area, with the origin in the bottom edge of the gauge area.

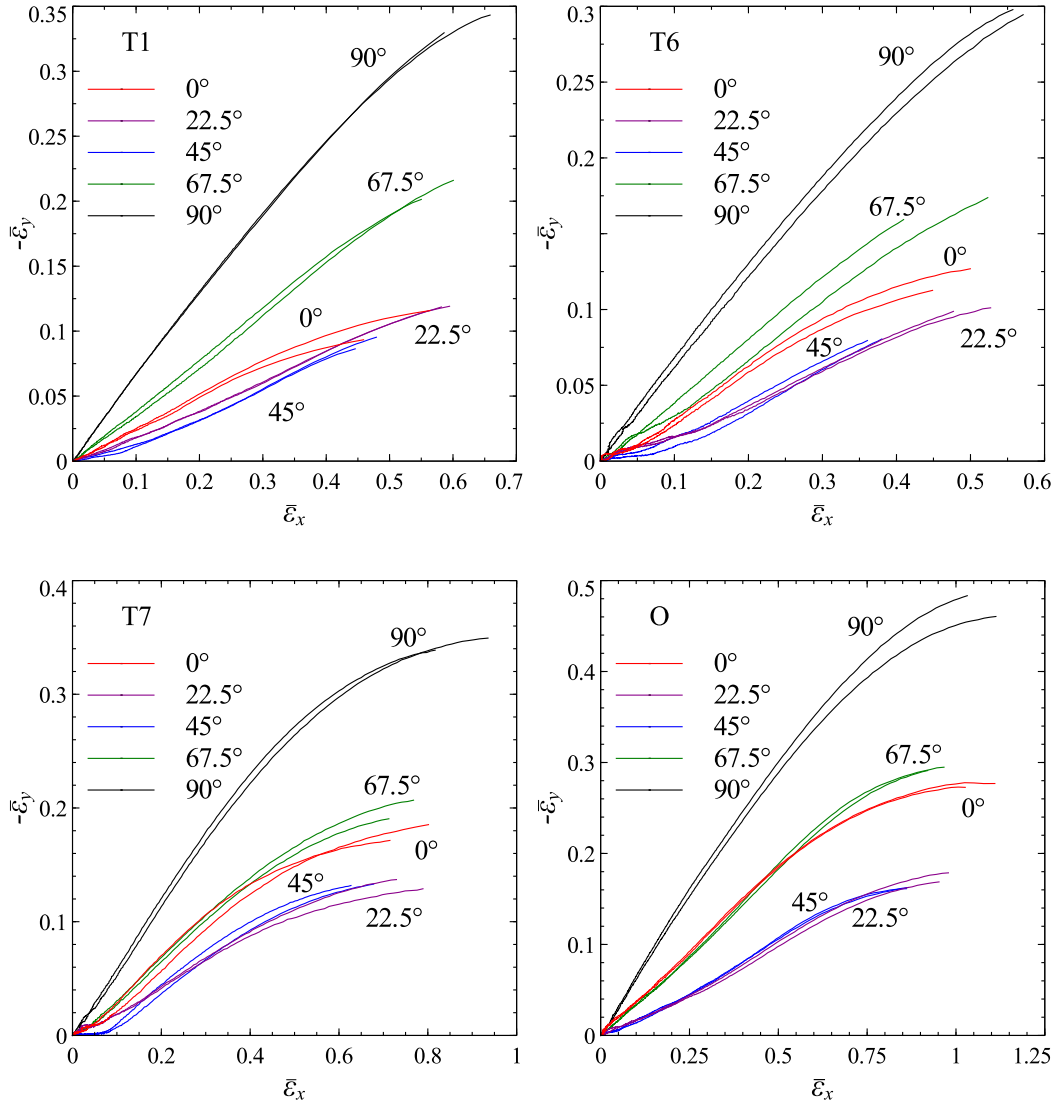

Figure 9: Negative average logarithmic strain in the width direction, $-\bar{\varepsilon}_y$, vs. average logarithmic strain in longitudinal direction, $\bar{\varepsilon}_x$, for all tempers and specimen orientations.

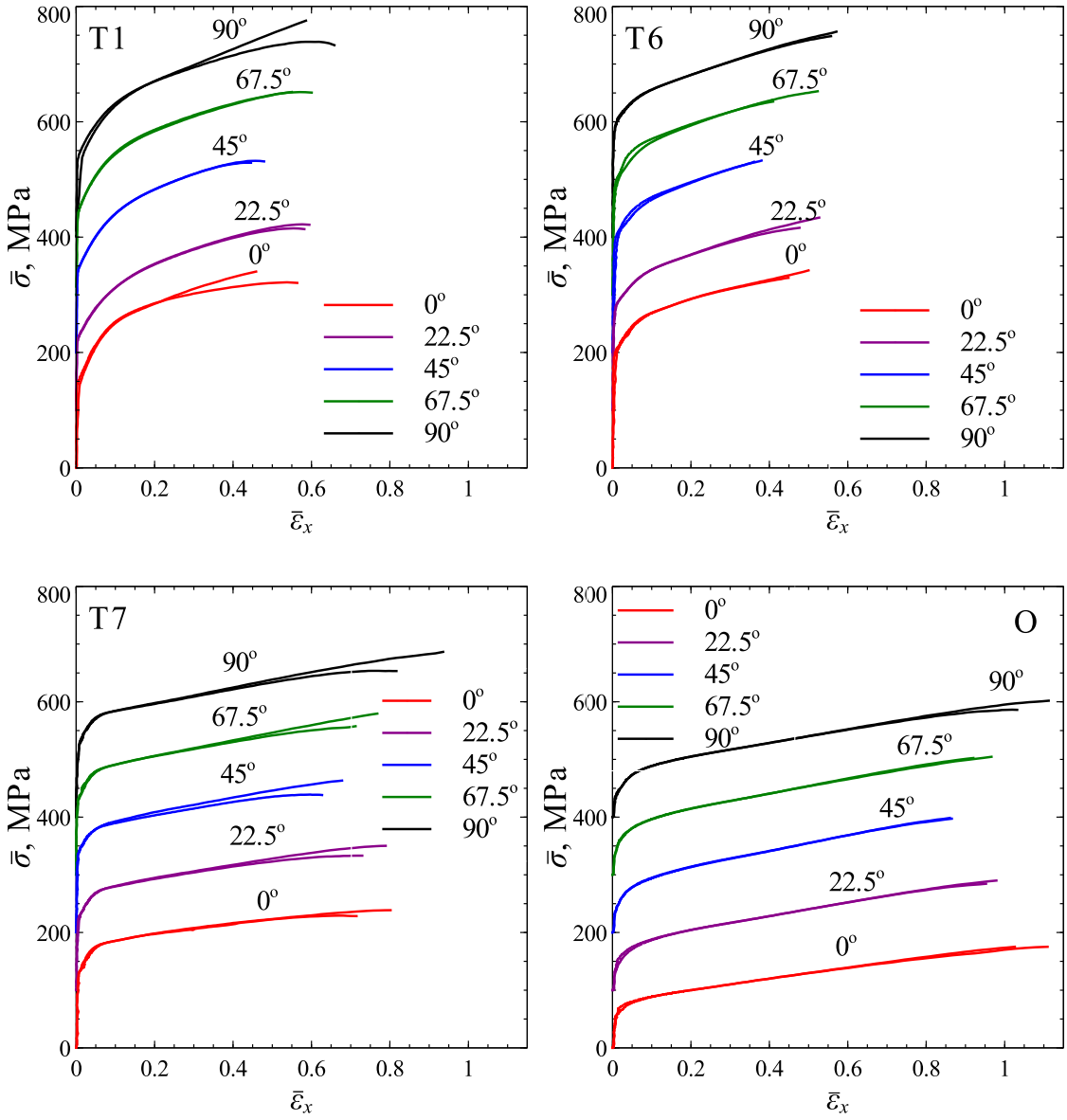

Figure 10: Stress-strain curves for all tempers and specimen orientations in terms of the stress $\bar{\sigma}$, and the average logarithmic tensile strain, $\bar{\varepsilon}_x$, at the surface of the specimen inside the neck region. Note that the curves for the different orientations are plotted with a 100 MPa offset from each other.

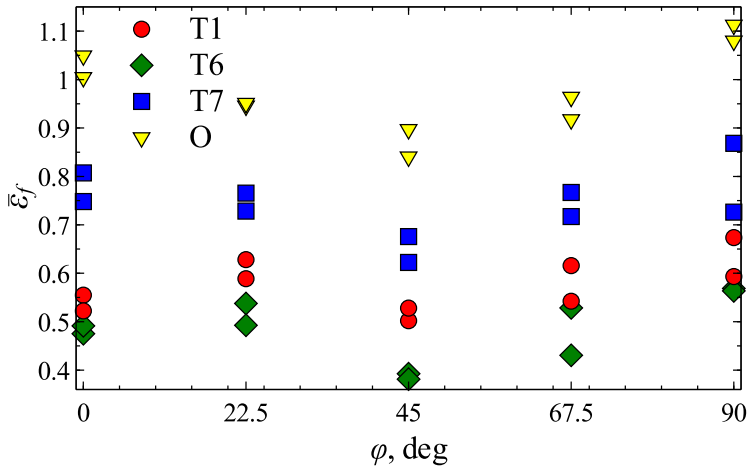

Figure 11: Average logarithmic tensile strain in the neck area at fracture, $\bar{\varepsilon}_f$, plotted against the tensile direction, φ.

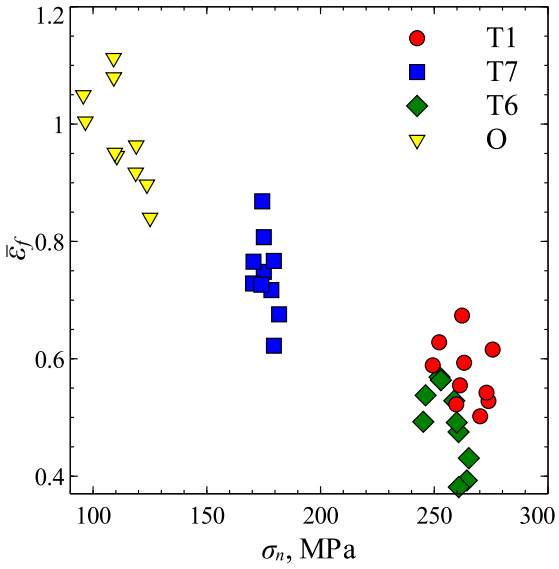

Figure 12: Average logarithmic tensile strain in the neck area at fracture, $\bar{\varepsilon}_f$, vs. true stress at necking, σ_n, for all tempers and specimen orientations.

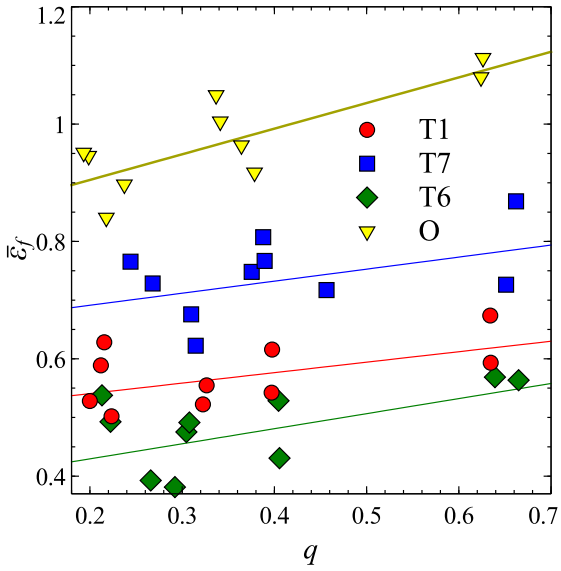

Figure 13: Average logarithmic tensile strain in the neck area at fracture, $\bar{\varepsilon}_f$, vs. the strain ratio, q, for all tempers and specimen orientations.

730

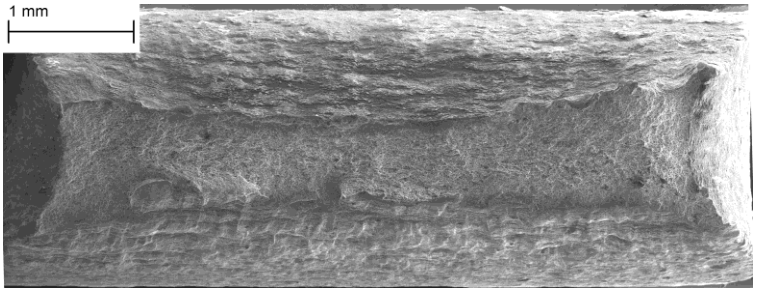

(a)

(b)

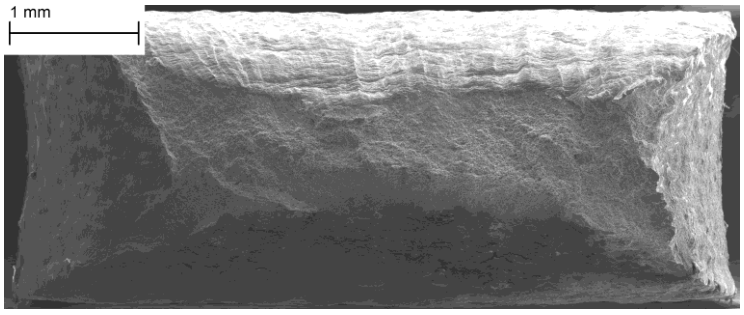

(c)

Figure 14: SEM images of the fracture surface of the specimens in O temper: a) 0° orientation, b) 45° orientation and c) 90° orientation.

735

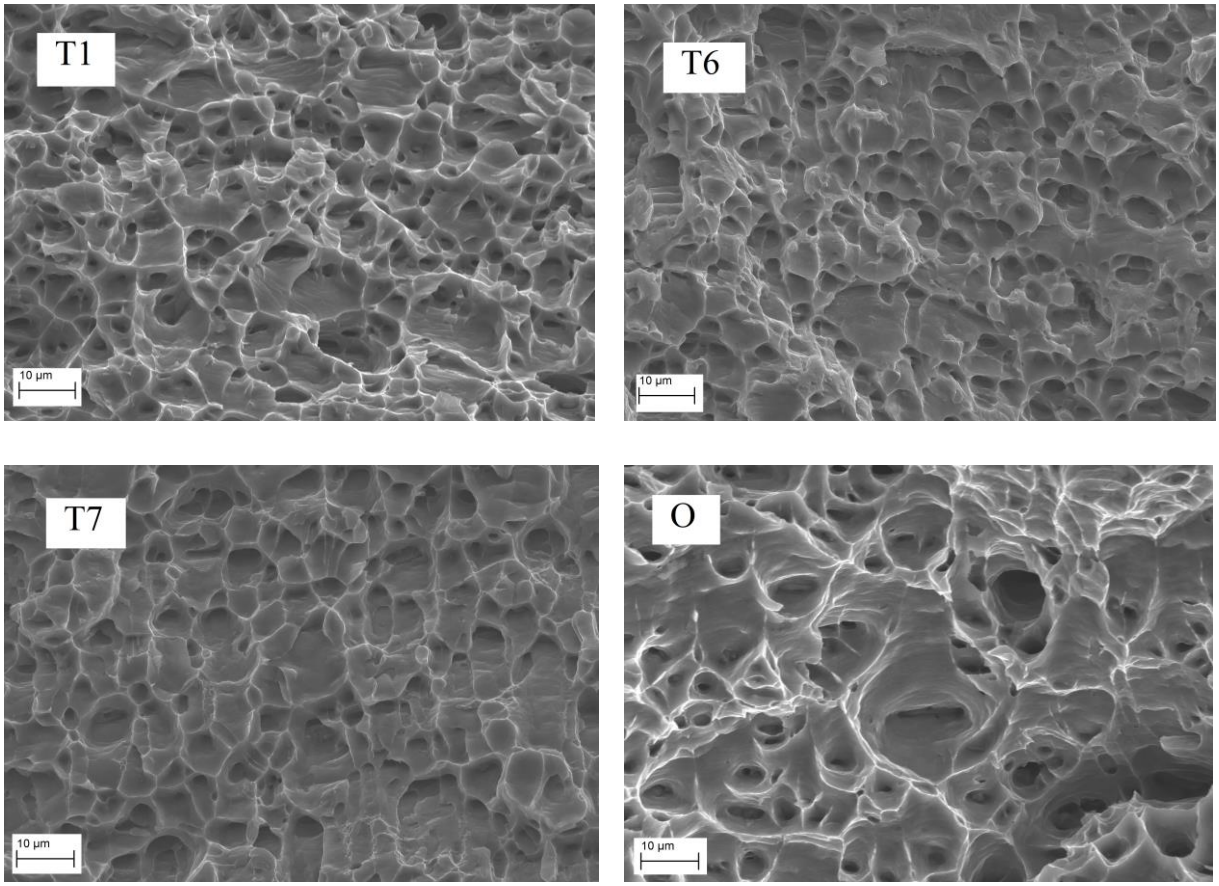

Figure 15: SEM images taken at approximately 1000 times magnification in the centre of the fracture surfaces of the 0° specimens.

740

745